# Time-of-arrival estimation by UWB radios with low sampling rate and clock drift calibration ☆

Y. Wang [a],[*], G. Leus [b], H. Deliç [c]

[a] Department of Automation, Shanghai Jiao Tong University, Shanghai 200240, PR China
[b] Faculty of Electrical Engineering, Mathematics, and Computer Science, Delft University of Technology, Mekelweg 4, 2628CD Delft, The Netherlands
[c] Department of Electrical and Electronics Engineering, Bogaziçi University, Bebek 34342, Istanbul, Turkey

## ARTICLE INFO

## ABSTRACT

In this paper, we propose a time-of-arrival (TOA) estimation scheme using impulse-radio ultra-wideband (IR-UWB). This scheme is featured by a low sampling rate and is robust against clock drift. Low-rate stroboscopic sampling, which can achieve an equivalent sampling rate as high as the Nyquist sampling rate, is adopted to achieve a high resolution TOA estimate by IR-UWB. Since a long preamble is required to collect sufficient data samples, the clock drift is one of the main error sources in TOA estimation with stroboscopic sampling IR-UWB systems. Taking the drift into account, we first obtain a maximum-likelihood (ML) estimate of the drift, and then estimate the TOA using the averaged data samples calibrated for the drift. Simulation results corroborate that the associated drift calibration significantly reduces the TOA estimation errors, and that stroboscopic sampling can achieve the same estimation resolution as Nyquist rate sampling.

## 1. Introduction

Impulse radio ultra-wideband (IR-UWB) is a promising technology for high resolution time-of-arrival (TOA) estimation [2–7]. It enables precise ranging and accurate positioning, which has a wide range of applications such as environment monitoring and control, target tracking, industrial quality control and emergency services [8–10]. To detect the first arriving component of IR-UWB in a dense multipath environment, we need to estimate its TOA with high accuracy.

Due to the large bandwidth of IR-UWB, its multipath components are resolvable, which is a benefit for accurate TOA estimation. However, for the same reason, the IR-UWB system requires a Nyquist sampling rate of several GHz, which is prohibitively high for a practical implementation [11,12]. Most ranging systems (e.g., [2,13]) are based on Nyquist rate sampling in order to take full advantage of the large bandwidth of IR-UWB to achieve a high ranging accuracy. Others choose to sacrifice the estimation accuracy for sub-Nyquist sampling, and make use of the outputs of analog correlators or energy detectors to extract timing information [14–21]. For example, energy detection is employed in [6,16,20] to generate energy samples at a sub-Nyquist sampling rate. As a result, the noise is squared, which causes a signal-to-noise ratio (SNR) penalty [22]. Furthermore, the TOA estimation performance in [6,16,20] degrades as the sampling rate decreases. More recently, there is a considerable drive to recover the

transmitted IR-UWB signals, which are sparse in the time domain, based on a relatively small number of samples obtained via compressive sampling (CS) at rates lower than what is prescribed by Nyquist [23]. However, because of the dense multipath environment, the received IR-UWB signals may have tens or hundreds of multipath components, a situation where CS may not be suitable.

In this paper, we follow a different way to reduce the sampling rate: we make use of stroboscopic sampling, which is widely used in channel probing [24]. It can obtain an effective sampling rate as high as several GHz using a low-rate analog-to-digital converter (ADC) running at several tens or hundreds of MHz with the penalty that the same waveform has to be repetitively transmitted. Since we have to transmit several identical pulses in order to collect the same number of samples as when transmitting one pulse sampled by an equivalent high sampling rate, the preamble for ranging is long. This longer preamble is the price we pay to merge a high ranging accuracy with a low sampling rate. On the other hand, different from the earlier mentioned energy detector based schemes [6,16,20], the frame samples obtained by stroboscopic sampling can be averaged to further suppress the noise. Hence, this scheme can enjoy the benefit of an increased SNR.

Further, whenever we consider TOA estimation for ranging, the clock plays an essential role. Due to the randomness of the clocks, the clock drift, which refers to the phenomenon where the clock does not run at the nominal frequency, becomes one of the main sources of error in range computation, and hence TOA estimation [3,25]. The problem is more severe in a stroboscopic sampling system, since it needs more time to collect sufficient samples. Although a symmetric double-sided two-way ranging (SDS-TWR) protocol as presented in [3,4] can reduce the ranging error due to clock drift significantly, it cannot calibrate for the TOA estimation error caused by the clock drift. The protocol only works well under the assumption that the TOA is estimated correctly. A delay-locked-loop (DLL) circuit is used in [25] to lock the clock frequency of the ranging responder to the estimated clock of the ranging initiator. However, a DLL may not be appropriate for a stroboscopic sampling scheme, since the responder and the initiator employ different clock frequencies. A trellis-based maximum likelihood (ML) crystal drift estimator is introduced in [26,27] to solve this problem. But the system samples at the Nyquist rate, which is still as high as several GHz. Furthermore, it assumes coarse synchronization with known code phase; but in reality, code mismatch will inevitably occur due to the clock drift and the unknown TOA. Therefore, we design a ranging preamble, solve the code mismatch problem and apply an ML estimator (MLE) to determine the clock drift in our stroboscopic sampling IR-UWB system. After the drift calibration, two TOA estimation methods, namely the peak selection (PS) and the jump back search forward (JBSF) method, are investigated considering performance and cost. In the preliminary work [1], only the PS method is used. However, the PS method cannot achieve a satisfying accuracy due to the channel properties. Therefore, we further investigate the JBSF method

and shed light on the relation between the parameter selection and the TOA estimation performance. Consequently, we calibrate for the timing error caused by the clock drift and achieve an accurate TOA estimate using a low sampling rate. In summary, the main contributions of this work are:

1. the use of stroboscopic sampling to reduce the sampling rate, but still obtain accurate TOA estimation, at the price of a longer preamble;
2. the design of a ranging preamble and algorithm for clock drift estimation that is robust against the code phase;
3. the evaluation of the impact of drift estimation on TOA estimation using the PS and JBSF methods.

The rest of this paper is organized as follows. In Section 2, we will first introduce the stroboscopic sampling principle. The clock drift is taken into account in the system model and the preamble is designed to facilitate the drift calibration. In Section 3, we propose a method to accurately estimate the TOA with drift calibration. Simulation results are shown in Section 4. Conclusions are drawn at the end of the paper.

Notation: We use upper (lower) bold face letters to denote matrices (column vectors). $x(\cdot)$ ($x[\cdot]$) represents a continuous (discrete) time sequence. $[\mathbf{X}]_{m,n}$, $[\mathbf{X}]_{m,:}$ and $[\mathbf{X}]_{:,n}$ denote the element on the $m$th row and $n$th column, the $m$th row, and the $n$th column of the matrix $\mathbf{X}$, respectively. $[\mathbf{x}]_n$ indicates the $n$th element of $\mathbf{x}$. $\mathbf{0}_m$ ($\mathbf{1}_m$) is an all-zero (all-one) column vector of length $m$. Moreover, $(\cdot)^T$, $|\cdot|$, $\|\cdot\|_F$ and $\star$ designate transposition, absolute value, Frobenius norm and convolution, respectively. $\lfloor x \rfloor$ and $\lceil x \rceil$ represent the largest integer smaller than or equal to $x$ and the smallest integer larger than or equal to $x$, respectively. All other notation should be self-explanatory.

## 2. System model

The preamble for ranging is composed of many frames. Each frame period $T_f$ holds one pulse. We design $T_f$ to be larger than the delay spread of the channel in order to avoid inter-frame interference (IFI). The receiver employs a front-end filter to select the band of interest as shown in Fig. 1. In general, we specify the filter in the frequency domain to capture most of the signal energy in the band of interest. The bandwidth $B$ of the front-end filter is quite large because of the bandwidth of the UWB signal. Hence, the Nyquist sampling rate becomes prohibitively high. Therefore, we resort to stroboscopic sampling [24] to sample the output of the front-end filter at rate $1/T_{\text{sam}}$, which is much smaller than its Nyquist sampling rate $2B$, i.e., $T_{\text{sam}} \geq 1/(2B)$. As we apply stroboscopic sampling, several identical frames have to be transmitted in order to collect a sufficient number of samples that are equivalent to those obtained by sampling one frame at a higher rate, which is defined as $1/T_b$ and satisfies the condition $T_b \leq 1/(2B)$ in order to prevent frequency aliasing. The resolution of TOA estimation, which is the smallest
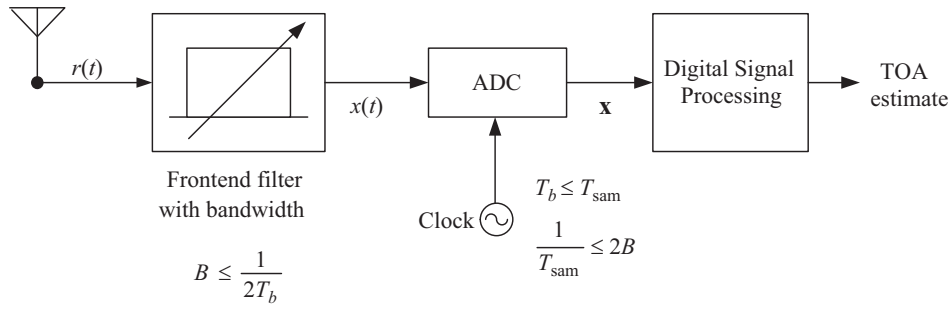
**Fig. 1.** The receiver's analog front-end. The output of the front-end filter is sampled at rate $1/T_{sam}$, which is smaller than its Nyquist sampling rate $2B$.

resolvable time difference, is determined by the equivalent sampling period $T_b$ ($\leq T_{sam}$). The sample vector **x** in Fig. 1 is the input of a digital signal processing (DSP) block. The DSP block accomplishes TOA estimation with clock drift calibration.

We remark here that the ADC used in stroboscopic sampling is comparable to one subconvertor of a time-interleaved ADC [28], which employs multiple subconvertors running at low rate in parallel to achieve an overall high sampling rate. Ideally, the resolution of TOA estimation using a time-interleaved ADC and stroboscopic sampling should be the same. They make different trade-offs between the sensing time and the hardware cost. In general, the ADC starts with a sample-and-hold (S/H) operation followed by quantization. In the case of stroboscopic sampling, the S/H circuit has to be fast enough to follow the change of the UWB signal [29]. The aperture jitter or aperture uncertainty of the ADC [30], which refers to the random variation of the sampling instant, should be negligible compared to the equivalent sampling period $T_b$ [31]. For example, if the targeted equivalent sampling period $T_b$ is 1 ns, the aperture jitter should be limited to a few picoseconds, which is feasible as reported in [11]. Moreover, since the stroboscopic sampling only employs one subconvertor, it would not suffer from the subconvertor mismatch problem, which imposes a big challenge to the time-interleaved ADC [32].

The relationships among $T_{sam}$, $T_f$, and $T_b$ are given as follows:

$$T_{sam} = mT_b, \tag{1}$$

$$T_f = (mP + q)T_b, \tag{2}$$

$$\frac{T_f}{T_b} = m\frac{T_f}{T_{sam}}, \tag{3}$$

where $m \geq 1$ is the sampling-rate gain, $P = \lfloor T_f/T_{sam} \rfloor$ is the minimum number of samples collected from one frame through stroboscopic sampling, and $m > q \geq 0$. These parameters are all integers. Moreover, $m$ and $mP + q$ should be relatively prime. Under the condition that $m=1$ and $q=0$, the system becomes a Nyquist sampling system. When designing the sampling-rate gain $m$, we would like it to be as large as possible to lower the sampling rate. On the other hand, it has to be small to shorten the preamble in order to save transmission energy. So there clearly is a design trade-off. Using $m$ frames to collect $mP + q$ samples is equivalent to sampling one frame at rate $1/T_b$.

The relative clock drift between the transmitter and the receiver violates the relation in (2). That is because $T_f$ is with respect to (w.r.t.) the transmitter, while $T_{sam}$ is w.r.t. the receiver. Since the relative clock drift ratio can be as large as 80 ppm [3], the drift of the preamble can lead to serious problems in TOA estimation. For instance, let us employ the system parameters in [20], where the symbol period is $T_{sym} = 3974.4$ ns, the number of symbols in the synchronization preamble (SYNC) is $N_{SYNC} = 1024$, and the number of symbols at the start of the frame delimiter (SFD) is $N_{SFD} = 64$. Assuming a clock drift ratio $\Delta$ of 80 ppm, a timing offset of 346 ns would be introduced after the synchronization header (SHR) (($N_{SYNC} + N_{SFD}$) $T_{sym}\Delta = 346$ ns). Even only considering the SFD part would cause a timing offset of 20 ns as well ($N_{SFD}T_{sym}\Delta = 20$ ns). Therefore, we have to calibrate for the clock drift at the receiver in order to obtain accurate ranging.

Assuming the clock drift ratio at the transmitter relative to the receiver $\Delta$ remains constant, the clock drift increases linearly with time. In order to suppress the noise and simplify the problem, we define a group of frames as a cluster according to the prior knowledge of the maximum drift ratio. The duration of a cluster is assumed smaller than the minimum time period required to observe a drift of $T_b$. Therefore, relation (2) is roughly maintained within the cluster. Recalling that $1/T_b$ is larger than $2B$, a maximum drift of $T_b$ within a cluster is much smaller than the width of the pulse, which is one of the parameters to decide the bandwidth of the UWB system. Hence, frame samples can be averaged over the cluster without severe pulse mismatch. The cluster period is defined as $N_f T_f$, where $N_f = mM$ and $M > 0$ is the processing gain. It has to satisfy the condition

$$N_f T_f \Delta_{max} = mMT_f \Delta_{max} \leq T_b, \tag{4}$$

where $\Delta_{max}$ is the maximum clock drift ratio at the transmitter relative to the receiver [26,27]. The outcome of the cluster averaging is $mP + q$ samples of one frame.

In order to achieve TOA estimation, we could design the preamble to be composed of several segments, each of which is dedicated to serve a different purpose, such as signal detection, coarse synchronization and fine synchronization. Each segment could have a different structure to facilitate its task. The structural design of the whole preamble is out of the scope of this paper. We assume that coarse synchronization has already been carried out. More specifically, we assume that the TOA $\tau$ is in the range of

one frame period w.r.t. the receiver, i.e., $\tau \in [0, (1+\Delta)T_f)$, where $(1+\Delta)T_f \approx T_f$, since the frame period $T_f$ is only several hundreds of ns and the clock drift ratio $\Delta \leq 80$ ppm. Therefore, we only concentrate on designing the preamble for the fine synchronization stage where $\tau$ is estimated. We assign a code chip to each cluster instead of each frame in order to avoid code mismatch during the averaging due to the unknown $\tau$ and the clock drift, which is not considered in [26,27]. We remark that the purpose of the code here is for spectrum smoothing and multiuser accessing, not for clock drift calibration, which can still work without any code assignment. Therefore, we do not consider the code design in this paper. Based on the analysis above, the structure of the transmitted preamble is shown in Fig. 2(a). The preamble is composed of $N_c$ clusters, where every cluster is made up of $N_f$ frames, each one containing one pulse. The transmitted signal can thus be written as

$$s(t) = \sum_{i=0}^{N_c-1} c_i b(t-iN_f T_f), \tag{5}$$

where $b(t) = \sum_{j=0}^{N_f-1} p(t-jT_f)$, $c_i$ is the cluster code chip ($c_i \in \{\pm 1\}$) and $p(t)$ is the transmitted pulse shape. Fig. 2 (b) and (c) show the noiseless received preamble through an ideal channel with unknown $\tau$ and different clock drifts. As we can observe from the figures, there is a code mismatch due to the unknown $\tau$ and the clock drift. The last (or first) several frames of the clusters in Fig. 2(b) (or Fig. 2(c)) are mismatched due to the unknown $\tau$ and the negative (or positive) drift. That is why we cut off the first and last $m$ frames of each cluster to get rid of the code mismatch in the averaging process at the price of reducing the processing gain from $M$ to $M-2$.

Through a multipath channel, the received preamble is given by

$$r(t) = \sum_{l=0}^{L-1} \alpha_l s(t-\tau_{l,0}-\tau, \Delta) + n(t), \tag{6}$$

where $L$ indicates the number of multipath components, $\alpha_l$ and $\tau_{l,0}$ respectively represent the amplitude and the relative time delay of the $l$th path with respect to the first path, $n(t)$ is zero-mean additive white Gaussian noise (AWGN) with double sided power spectral density $N_0/2$, and

$$s(t, \Delta) = \sum_{i=0}^{N_c-1} c_i b(t-iN_f T_f(1+\Delta), \Delta), \tag{7}$$

$$b(t, \Delta) = \sum_{j=0}^{N_f-1} p(t-jT_f(1+\Delta)). \tag{8}$$

Note that $\tau_{l,0} = \tau_l - \tau_0$, where $\tau_l$ is the multipath delay and $\tau_0 = \tau$. We remark that the frame period at the transmitter is $T_f$, and the one at the receiver is $T_f(1+\Delta)$. With the received signal $r(t)$, the output of the front-end filter sampled using stroboscopic sampling is

$$x(nT_{\text{sam}}) = \int_{-\infty}^{+\infty} r(t)g(nT_{\text{sam}}-t)\,dt, \quad n = 0, 1, \ldots, MN_c L_f, \tag{9}$$

where $g(t)$ is the impulse response of the front-end filter, whose bandwidth is large enough to include the band of interest, and $L_f = T_f/T_b = mP + q$ is the frame length in terms of the number of samples at rate $1/T_b$. Let us introduce $\mathbf{x}_k = [x(kL_f T_{\text{sam}}) \ldots x((kL_f + L_f - 1)T_{\text{sam}})]^T$, for $k = 0, 1, \ldots, N_c M - 1$, which is an $L_f$-long sample vector for the $k$th equivalent frame. Notice that $\mathbf{x}_k$ is the result of sampling $m$ frames at rate $1/T_{\text{sam}}$ at the receiver. Every $M$ sample vectors are grouped as a cluster. We exclude the first and last sample vectors in each cluster to get rid of the code mismatch in the averaging process. The results are collected in a data matrix $\mathbf{X}$ of size $L_f \times N_c$, which is given by

$$\mathbf{X} = \frac{1}{M-2} \left[ \sum_{i=1}^{M-2} \mathbf{x}_i \sum_{i=1}^{M-2} \mathbf{x}_{M+i} \cdots \sum_{i=1}^{M-2} \mathbf{x}_{(N_c-1)M+i} \right], \tag{10}$$

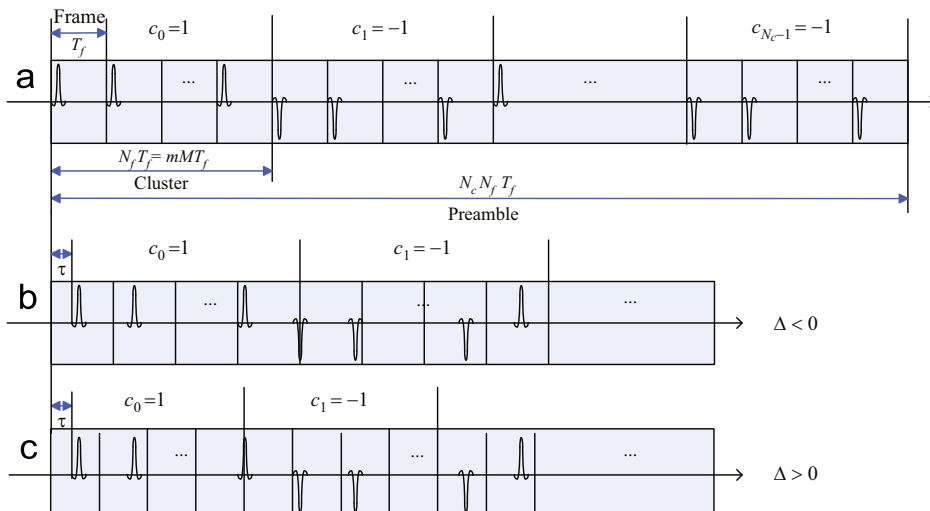where each column of $\mathbf{X}$ contains its own specific code chip.



**Fig. 2.** The structure of (a) the preamble, (b) the received preamble with negative drift, and (c) the received preamble with positive drift.

## 3. TOA estimation with clock drift calibration

### 3.1. Recovery from stroboscopic sampling

Due to the stroboscopic effects, we have to permute all the averaged frame samples in each column of $\mathbf{X}$ before we calibrate for the drift and estimate the TOA $\tau$. The adjacent $T_{sam}$−spaced samples obtained by stroboscopic sampling are not the adjacent $T_b$-spaced samples in the equivalent high sampling rate scheme. The maximum drift observed in a cluster is $T_b$, which is much smaller than the sample spacing $T_{sam}$ in the stroboscopic sampling scheme, and exactly equal to the sample spacing in the equivalent high sampling rate scheme. Therefore, we have to recover the equivalent high sampling rate sequence before drift calibration to appropriately represent the drift between the adjacent clusters. Recall that $m$ is the sampling-rate gain. According to (2), we define a permutation matrix $\mathbf{W}$ of size $L_f \times L_f$ with first column $[\mathbf{W}]_{:,1} = [1 \ \mathbf{0}_{L_f-1}^T]^T$ and every other column a circulant shift of the previous column with $m$ samples. This means that

$$[\mathbf{W}]_{:,i+1} = \text{circshift}([\mathbf{W}]_{:,i}, m), \quad i = 1, \ldots, L_f-1, \tag{11}$$

where circshift $(\mathbf{a}, n)$ circularly shifts the values in the vector $\mathbf{a}$ by $|n|$ elements (down if $n > 0$ and up if $n < 0$). The rearrangement is accomplished by

$$\mathbf{X}_o = \mathbf{W}\mathbf{X}, \tag{12}$$

where each column of $\mathbf{X}_o$ collects the permuted averages for each cluster. Now, the equivalent sample spacing in $\mathbf{X}_o$ is $T_b$.

### 3.2. Clock drift estimation

In order to estimate the TOA, we would like to use all the data samples in $\mathbf{X}_o$. This allows us to obtain an averaged sample vector over all the clusters and thereby reduce the noise. However, due to the clock drift, the equivalent frame waveforms are not aligned with each other. We have to calibrate for the drift before TOA estimation. Let us define the row index of the data matrix $\mathbf{X}_o$ as the frame phase, similar to the pulse repetition period (PRP) phase in [26,27]. We recall that the maximum drift accumulated over a cluster duration is $T_b$, and the difference between two adjacent phases is also $T_b$. We have assumed that the accumulated drift, which is the total drift observed over the duration from the beginning of the preamble to the time point of interest, is zero at the beginning of the preamble. The frame phase of a cluster may correspond to the same or an adjacent phase in the next cluster due to the accumulated drift. This kind of correspondence is called the transition between frame phases. The drift estimation traces the correct transition path of the frame phase within the duration of the preamble. A transition takes place between two contiguous clusters, when the accumulated drift exceeds $T_b$. The transition path pattern is generated by quantizing the accumulated drift over clusters. The quantization step size is $T_b$, and a ceiling quantization is employed. Every frame phase has the same set of transition paths. We remark that the exact number of the drift ratio is not the main concern,

but the transition path is the target of the drift estimation. Based on this path, we can calibrate for the drift, obtain an averaged sample vector for the whole preamble, and then estimate the TOA. The resolution of the drift estimation is $T_b/(N_f T_f(N_c-1))$. The total number of transition paths for each frame phase is $2N_c-1$, where $N_c-1$ is the path number for positive drift (or negative drift), and one path is reserved for the case without any drift. Therefore, the longer the preamble, the more accurate the drift estimation. Nevertheless, the complexity of the estimation would also increase as the number of transition paths increases.

Fig. 3 shows some examples of transition paths. In the example, $N_c=5$ and $L_f=13$. The dots represent the elements of the matrix $\mathbf{X}_o$. The spacing between contiguous samples is $T_b$. Based on Fig. 3, we reconfirm that the data matrix $\mathbf{X}$ cannot be used directly. Some of the transition paths for frame phase 7 are shown. As mentioned before, we have assumed that the accumulated drift at the beginning of cluster 1 is zero. Path 1 indicates that we can observe a phase transition for every cluster, and the $k$th phase of the $i$th cluster transfers to the $(k-1)$th phase of the $(i + 1)$th cluster. It reaches the maximum negative drift, which is assumed as $-\Delta_{max}$. In path 5, no clock drift is observed. Path 6 shows a drift of $T_b$ over five clusters, which corresponds to a resolution of the drift ratio estimation given by $\Delta_{max}/4$. We remark that path 6 is the only transition path that can observe a positive drift of $T_b$ over five clusters, according to the quantization rules and the assumption of the zero accumulated drift at the start of the preamble. The number of all possible transition paths for each frame phase is $2N_c-1 = 9$. There are special cases we have to be careful with. For example, in path $a$ for phase 2, there is a negative shift of one phase every cluster. Therefore, phase 1 of cluster 2 transfers to phase 13 of cluster 3 as shown by the dashed line with solid arrows in the figure. Meanwhile, path $b$ (the dashed line with hollow arrows) for phase 10 describes a positive shift of one phase every cluster and propagates in a similar way as path $a$. The transition takes place circularly. Since we have excluded the code mismatch during the cluster averaging process by cutting off the first and last sample vectors, each column of $\mathbf{X}_o$ corresponds to its own specific code chip. However, the phase mismatch due to the clock drift still causes serious problems for TOA estimation.

All the transition paths for any phase are modeled by a matrix $\mathbf{\Lambda}$ of size $(2N_c-1) \times N_c$. For $N_c=5$, $\mathbf{\Lambda}$ is shown as an example at the right side of Fig. 3. The path number in Fig. 3 corresponds to the row index of $\mathbf{\Lambda}$. Making use of the transition matrix and recalling the cluster code, we can estimate the transition path and calibrate for the clock drift. Since all the phases have the same set of transition paths, we perform an exhaustive search of the transition path that collects the maximum energy over the whole preamble in order to be more robust to noise, which can be regarded as the MLE for the clock drift. Let us define $j_{max}$ as the row index of the selected path in $\mathbf{\Lambda}$. Based on the above discussions, the estimate of $j_{max}$ is given by

$$j_{max} = \arg \max_{j \in \{1, \ldots, 2N_c-1\}} \sum_{k=1}^{L_f} \left\| \sum_{n=1}^{N_c} c_{n-1}[\mathbf{X}_o]_{p(k,n,j),n} \right\|_F^2, \tag{13}$$
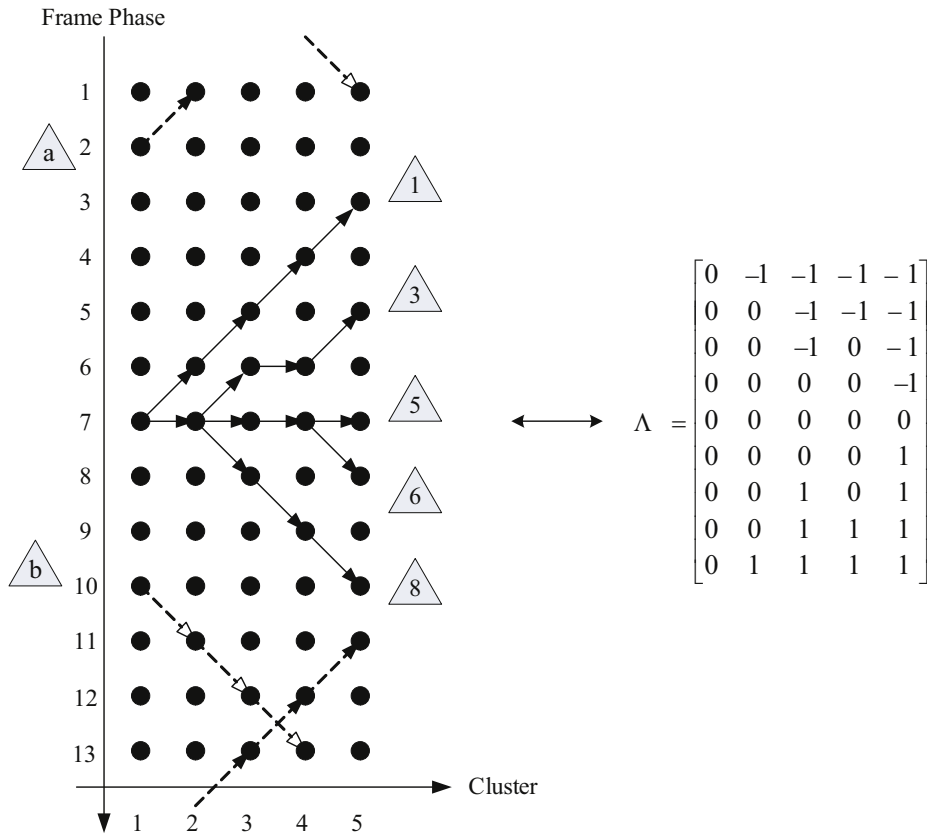
Frame Phase



**Fig. 3.** The diagram of the transition paths and the corresponding matrix $\Lambda$ for $N_c = 5$ and $L_f = 13$.

where

$$p(k,n,j) = \mathrm{mod}\left(\left(k-1 + \sum_{i=1}^{n} \Lambda(j,i)\right), L_f\right) + 1, \qquad (14)$$

with $\mathrm{mod}(a,b)$ representing $a$ modulo $b$. The clock drift ratio corresponding to the selected transition path can be estimated as

$$\hat{\Delta} = \frac{(j_{\max} - N_c)T_b}{(N_c - 1)N_f T_f}. \qquad (15)$$

Note that in the above procedure, we only estimate the clock drift. In order to obtain a lower computational complexity, we decouple the drift calibration and the TOA estimation to handle them sequentially. We remark that the complexity of the drift estimator depends on the search space, which has $2N_c - 1$ possible paths in total. We do not take the complexity of the comparison into account, ignore the code multiplication, and do not consider the optimal search strategy. In the worst case scenario, we carry out an exhaustive search over all the possible paths. To calculate the energy collected through the path over the whole preamble, we need $L_f N_c$ operations. Thus, the operations required by the clock drift estimator are in the order of $O(L_f N_c(2N_c - 1))$. On the other hand, we can also jointly consider drift calibration and TOA estimation based on different TOA estimation techniques. A simple joint approach is to estimate the clock drift and the strongest multipath component at the same time. However, it requires a two-dimensional search. Moreover, in a none-line-of-sight (NLOS) scenario, the first multipath

component is in general not the strongest one, so looking for the strongest path is not always the best option for TOA estimation. Therefore, we focus on the decoupled approach for low complexity and high flexibility.

### 3.3. TOA estimation

So far we have estimated the transition path for the clock drift using (13). Before we continue to discuss the TOA estimation strategies, we first average the related phases of $\mathbf{X}_o$ over the whole preamble according to the transition path $\Lambda(j_{\max}, :)$ to calibrate for the drift and further mitigate the noise, and collect the outcomes in a sample vector $\mathbf{y}$, which is actually a circularly shifted version of the channel estimate. Its elements are computed as

$$[\mathbf{y}]_k = \frac{1}{N_c} \sum_{n=1}^{N_c} c_{n-1}[\mathbf{X}_o]_{p(k,n,j_{\max}),n}, \quad k = 1, 2, \ldots, L_f. \qquad (16)$$

The vector $\mathbf{y}$ is used for TOA estimation. As a result, the total processing gain for TOA estimation is $N_c(M-2)$.

We define $k_{\max}$ as the index of the strongest multipath component, which is found by

$$k_{\max} = \arg \max_{k \in \{1,2,\ldots,L_f\}} |[\mathbf{y}]_k|. \qquad (17)$$

Thus, the TOA estimate according to the peak selection (PS) method [13,14] is given by $\hat{\tau}_{PS} = T_b k_{\max} - T_b/2$. In a NLOS scenario, the problem to detect the leading edge arises, since the first path may not be the strongest one. Therefore, we resort to the jump back and search forward

(JBSF) method, which relies on two parameters, the threshold $\gamma$ and the search back window length $L_w$. It first aligns with the strongest component, and then jumps back to start from the index of $k_{max} - L_w$ to find out the first $|[\mathbf{y}]_k|$ exceeding the threshold $\gamma$. It can be summarized as

$$\hat{\tau}_{JBSF} = T_b \min\{k \in \{k_{max} - L_w, k_{max} - L_w + 1, \ldots, k_{max}\} |$$
$$|[\mathbf{y}]_{k \bmod L_f}| > \gamma\} \qquad (18)$$

Note that since $k_{max} - L_w$ can be negative, we use the circularly shifted index $k \bmod L_f$ instead of the negative index. An example of how these TOA estimation strategies can be applied to $\mathbf{y}$ is shown in Fig. 4. In the example, the search back window includes both the head and the tail of the frame, as $k_{max} - L_w < 0$. We observe that the TOA estimate obtained by the JBSF method is the closest to the true TOA. Furthermore, we remark that the complexity of the TOA estimator is negligible compared to the clock drift estimator. The number of operations required for TOA estimation is proportional to the search space, which contains $L_f$ candidate TOA estimates.

The challenge in the threshold-based TOA estimation is imposed by the unknown statistical properties of the channel. The optimal way to detect the leading edge would be a likelihood ratio test (LRT) for multiple hypotheses [33]. However, this requires full statistical knowledge of the channel, which is impractical. In the absence of channel information or lack of sufficient channel information, we could follow a heuristic approach and set the threshold to $\gamma_1 = \eta_t |[\mathbf{y}]_{k_{max}}|$, where $0 \le \eta_t \le 1$ is the threshold ratio [34]. However, the optimal $\eta_t$ would depend on the SNR in this scheme and there is no unique $\eta_t$ that works well under all SNRs. On the other hand, we could set the threshold based on the stochastic properties of $\mathbf{y}$, when there is only noise. A threshold can be derived for a fixed probability of early false alarm $P_{EFA}$, which indicates the event where we incorrectly select a noise sample before the true TOA as the first multipath component. If there is no absolute sample value exceeding the threshold in the predefined window, we use the result of the PS method as the estimated TOA. When there is only noise, $[\mathbf{y}]_k$ is

an averaged AWGN sample with variance $\sigma^2 = N_0 B / (N_c(M-2))$, i.e. $[\mathbf{y}]_k \overset{a}{\sim} \mathcal{N}(0, \sigma^2)$. This means $|[\mathbf{y}]_k|$ follows a one-degree chi distribution (half-normal distribution), i.e. $|[\mathbf{y}]_k| / \sigma \overset{a}{\sim} \mathcal{X}_1$. As a result, we can design a threshold $\gamma_2$ according to

$$P_{EFA} = P(|[\mathbf{y}]_k| > \gamma_2; \text{ noise only}) = 2Q\left(\frac{\gamma_2}{\sigma}\right), \qquad (19)$$

which leads to

$$\gamma_2 = \sigma Q^{-1}\left(\frac{P_{EFA}}{2}\right), \qquad (20)$$

where the function $Q(\cdot)$ is the right-tail probability function for a Gaussian distribution.

The length $L_w$ of the backward search window should be large enough to recover the first path instead of dead-locking to the strongest one, and it depends on the delay between the strongest path and the first path, which could be as large as 60 ns for the IEEE 802.15.4a channel model CM1 [35], as shown in [15]. Due to the lack of channel knowledge, we choose $L_w$ to be $\eta_l T_f$, where $0 \le \eta_l \le 1$ is the length ratio. We remark that $T_f$ should also be long enough, not only to avoid IFI but also to accommodate enough margin for the backward search window in order to prevent the window from including the channel tail. Therefore, $T_f$ should be decided by the delay spread of the channel and the maximum delay between the strongest path and the first path together. For example, if we assume that the channel length is 90 ns and the maximum delay between the first path and the strongest path is 60 ns, $T_f$ should be at least 150 ns.

## 4. Simulation results

The performance of TOA estimation is evaluated by simulations using the IEEE 802.15.4a channel model CM1 – indoor residential LOS [35]. One hundred channel realizations are generated, and we randomly choose one for each Monte Carlo run. To speed up the simulations, we generate the output of the cluster averaging process directly, since the maximum drift of $T_b$ within a cluster is smaller than the pulse width. The averaging process would not suffer from severe pulse mismatch as we mentioned before. $E_c/N_0$ defines the cluster energy to noise variance ratio. The number of clusters $N_c$ is 68. Further, we randomly select the drift ratio $\Delta$ among {−67.2 ppm, −50.4 ppm, −33.6 ppm, −16.8 ppm, 0 ppm, 16.8 ppm, 33.6 ppm, 50.4 ppm, 67.2 ppm} in each run. Since the channel length is no longer than 90 ns and the maximum delay between the first path and the strongest path is 60 ns for CM1 [15], the frame period is set as the sum of the channel length and the maximum delay based on the design principle discussed in Section 3.3, i.e., $T_f = 150$ ns. The stroboscopic sampling period $T_{sam}$ is chosen to be 7 ns. The targeted resolution $T_b$ is 1 ns. Based on (2), we obtain $P = 21$, $m = 7$ and $n = 3$. The maximum $M$ is 12 according to (4). The number of frames in one cluster is $N_f = mM = 84$. Therefore, the processing gain of the cluster averaging process is $M - 2 = 10$, or approximately 10 dB. The total processing gain is $N_c(M-2) = 680$, or approximately 28 dB, and the total length of the preamble is $N_c N_f T_f = 856.8$ μs.
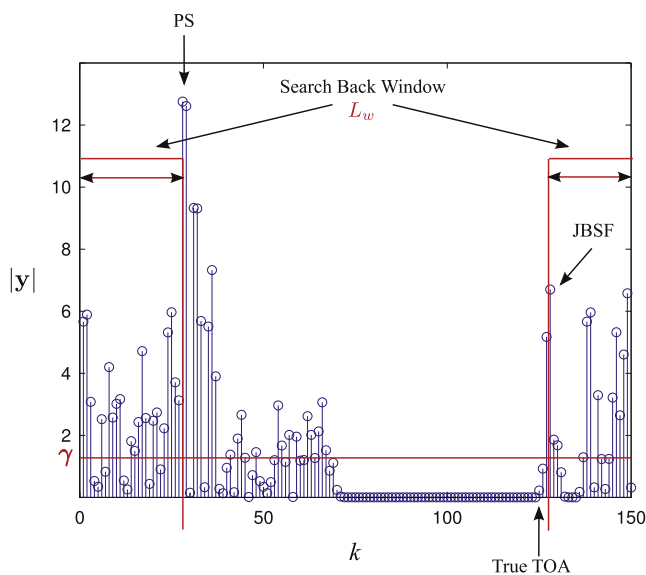


**Fig. 4.** An example of applying different TOA strategies to noiseless $|\mathbf{y}|$.

According to the IEEE 802. 15.4a standard [3], the duration of the SHR preamble can be several thousands of microseconds (μs) (e.g. 1025.4 μs or 4422.6 μs). It indicates that our preamble design can be accommodated. When the SNR is high, we do not have to use so many clusters for averaging and the preamble length can be further reduced. Moreover, the timing offset $\tau \in [0, T_f)$ is randomly generated in each run. The threshold ratio is $\eta_t \in \{0.1, 0.2, \ldots, 0.8\}$. The length ratio of the backward search window is $\eta_l \in \{0.1, 0.2, \ldots, 0.7\}$, which leads to $L_w \in \{10 \text{ ns}, 20 \text{ ns}, \ldots, 70 \text{ ns}\}$.

In the simulations, an 8th order Butterworth pulse with a 3 dB bandwidth of 500 MHz is employed, similarly as in [20]. The center frequency $f_0$ is 4.5 GHz. In order to get rid of the noise outside the band of interest, the received signal is first filtered by a bandpass filter (BPF), whose center frequency is $f_0$ and bandwidth is 500 MHz. Then, the output of the BPF is down-converted by multiplying it with $e^{j2\pi f_0 t}$, and filtered by a low pass filter (LPF), which is also an 8th order Butterworth filter with a 3 dB bandwidth of 500 MHz. Since the received signal is split into I/Q branches, the recovery from stroboscopic sampling is carried out in each branch separately. Then, the drift calibration makes use of the data samples in both branches. Therefore, we adapt the path index estimate (13) as

$$j_{\max} = \arg \max_{j \in \{1, \ldots, 2N_c - 1\}} \sum_{k=1}^{L_f} \left\{ \left\| \sum_{n=1}^{N_c} c_{n-1} [\mathbf{X}_I]_{p(k,n,j),n} \right\|_F^2 \right.$$

$$\left. + \left\| \sum_{n=1}^{N_c} c_{n-1} [\mathbf{X}_Q]_{p(k,n,j),n} \right\|_F^2 \right\}, \tag{21}$$

where $\mathbf{X}_I$ and $\mathbf{X}_Q$ are from the I/Q branches, respectively. Accordingly, the averaged sample vector (16) is modified as

$$[\mathbf{y}]_k = \sqrt{\left\| \frac{1}{N_c} \sum_{n=1}^{N_c} c_{n-1} [\mathbf{X}_I]_{p(k,n,j_{\max}),n} \right\|^2 + \left\| \frac{1}{N_c} \sum_{n=1}^{N_c} c_{n-1} [\mathbf{X}_Q]_{p(k,n,j_{\max}),n} \right\|^2},$$

$$k = 1, 2, \ldots, L_f. \tag{22}$$

As a result, $[\mathbf{y}]_k$ follows a Rayleigh distribution. We obtain $[\mathbf{y}]_k \sim \text{Rayleigh}(\sigma/\sqrt{2})$, where $\sigma^2 = N_0 B / (N_c(M-2))$ and $R \sim \text{Rayleigh}(\sigma_o)$, with $R = \sqrt{X^2 + Y^2}$, $X \sim \mathcal{N}(0, \sigma_0^2)$ and $Y \sim \mathcal{N}(0, \sigma_0^2)$. We can calculate the threshold $\gamma_2$ corresponding to different $P_{\text{EFA}}$ based on the cumulative distribution function (CDF) of the Rayleigh distribution.

We first evaluate the performance of TOA estimation using the PS method, which consists of choosing the strongest component. The root mean square error (RMSE) of $\hat{\tau}_{PS}$ vs. $E_c/N_0$ is illustrated in Fig. 5. There are large performance gaps between the cases with drift calibration (solid lines) and the cases without drift calibration (dashed lines with "○" or "△" markers). The drift causes serious problems to TOA estimation as indicated by the high error floor for the curves without calibration for the whole SNR range. The Nyquist rate sampling system, where $m=1$ and $n=0$, is used as a reference. The same preamble is used for the Nyquist sampling system and the stroboscopic sampling system. No matter how large $m$ is, drift calibration always attains the same error floor for large enough $E_c/N_0$ (solid lines). Nyquist rate sampling gains about 8 dB over stroboscopic sampling ($m=7$) due to the sampling-rate gain $m$. The SNR penalty of the stroboscopic sampling is obvious. For both systems, we also show the performance
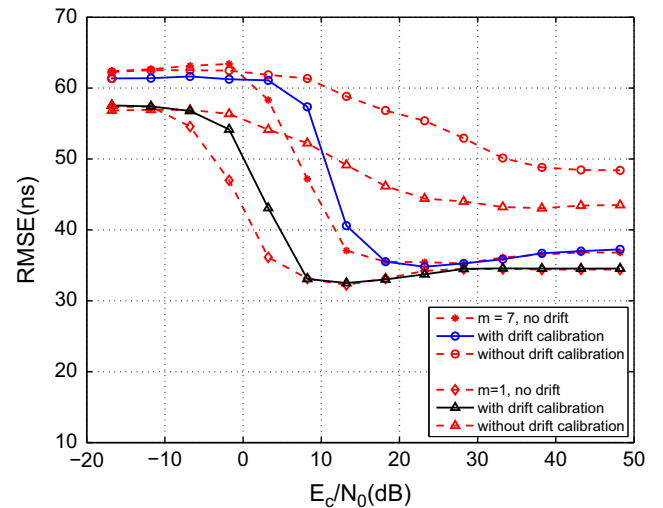

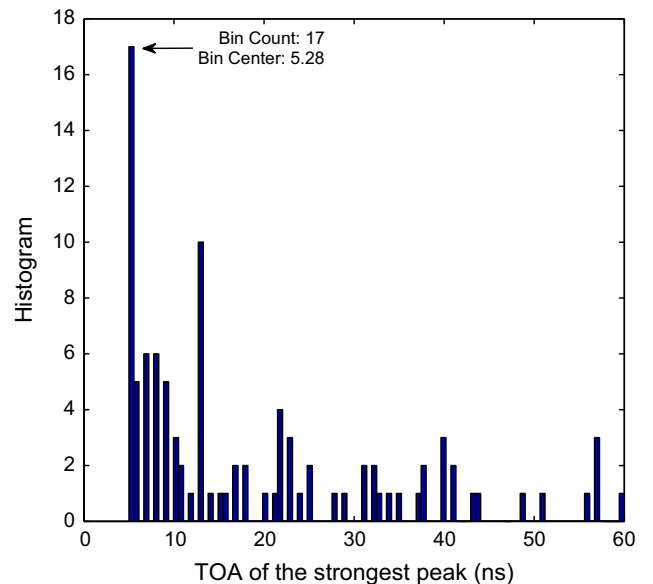
**Fig. 5.** RMSE of TOA estimation using peak selection.



**Fig. 6.** The histogram of the TOA of the strongest peak, without drift.

of the ideal case without any drift (dashed lines with "∗" or "◇" markers). They show similar error floors as the ones with drift calibration, which proves that the drift calibration performs quite well. Note that although the CM1 channel is for residential LOS, the first path is not always the strongest one. To clarify this, we further investigate the properties of the CM1 channels. With the assumption of no propagation delay ($\tau = 0$), Figs. 6 and 7 show the histograms of the TOA of the strongest peak of $\mathbf{y}$ without drift and with drift calibration, respectively. The histograms use 100 CM1 channel realizations and both figures are noiseless. As shown in Figs. 6 and 7, the strongest peak is not always the first peak. Therefore, the PS method may have a high error floor. Since $T_b = 1$ ns and CM1 is LOS, most peaks are expected to appear in the first bin. However, due to the pulse width, and the effect of the BPF and the LPF at the receiver, the earliest and strongest peaks shift to the bin at 5 ns. Moreover, the drift changes the histogram even with drift calibration as shown in
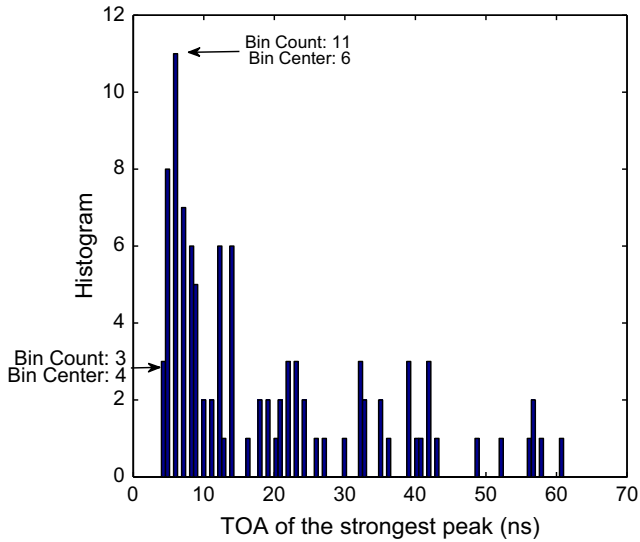
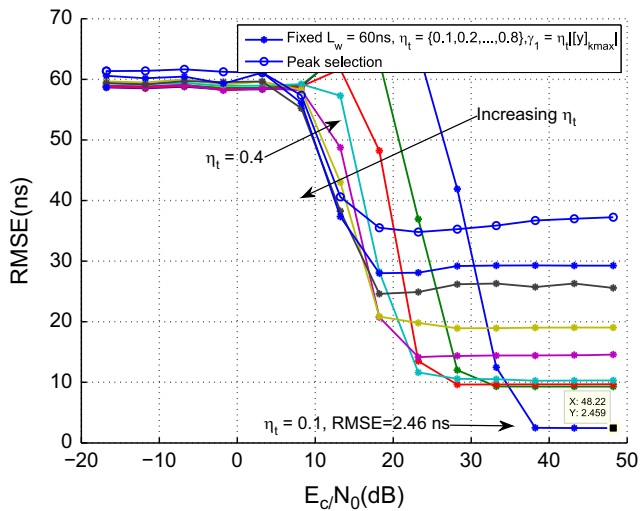**Fig. 7.** The histogram of the TOA of the strongest peak, with drift calibration.



**Fig. 8.** RMSE of TOA estimation using the JBSF method for a fixed window length $L_w = 60$ ns and different thresholds $\gamma_1 = \eta_t |[\mathbf{y}]_{k_{max}}|$, $m = 7$.

Fig. 7. The mean and the median of the TOA for the case without drift (Fig. 6) are respectively 23.50 ns and 12 ns, and the largest TOA is at 60 ns. Meanwhile, the mean and the median of the TOA for the one with drift calibration (Fig. 7) are respectively 23.64 ns and 11.51 ns, and the largest TOA is at 61 ns. They are slightly different. The properties of the CM1 channels indicate one of the reasons why the PS method may have a high error floor. Moreover, we obtained a circularly shifted frame waveform to estimate the strongest path. Once the strongest path is not the first path, large errors can also be introduced due to the circularly shift as shown in Fig. 4. In general, the performance of the PS method cannot fulfill the high accuracy requirement.

Consequently, we investigate the performance of TOA estimation using the JBSF method, which deals with the scenario where the first path is not the strongest and achieves much better accuracies than the PS method. Since the threshold and the length of the backward search window are the key parameters in the JBSF method,

we explore their impact on TOA estimation. Fig. 8 shows the RMSE of $\hat{\tau}_{JBSF}$ for a fixed window length $L_w = 60$ ns and different thresholds $\gamma_1 = \eta_t |[\mathbf{y}]_{k_{max}}|$, where $\eta_t$ is the threshold ratio defined in Section 3.3. There is no single threshold which could outperform the others over the whole SNR range. A smaller threshold can achieve a better accuracy at high SNR, but also performs worse at low SNR, which is consistent with the conclusions in [34]. The error floor of peak selection is higher than any error floor encountered by the JBSF method. Although $\eta_t = 0.1$ achieves the best performance at high SNR (2.46 ns), it does not maintain good performance for low and medium SNR. According to Fig. 8, the performance at $\eta_t = 0.4$ yields a good trade-off over the whole SNR range. It only has a 2 dB performance loss in the SNR range of 8–18 dB compared to larger thresholds, and its error floor is still close to the low error floors obtained by smaller thresholds. Furthermore, the performance of the JBSF method with a fixed threshold $\gamma_1 = 0.4|[\mathbf{y}]_{k_{max}}|$ and $\gamma_1 = 0.1|[\mathbf{y}]_{k_{max}}|$ under different backward search windows is shown in Figs. 9 and 10, respectively. In Fig. 9, the larger the window length, the smaller the error floor. The performance differences in the low SNR range are smaller than the ones with a fixed window length and various thresholds $\gamma_1$. There is no more performance improvement, when the window length is larger than 60 ns. Since we know that the maximum delay between the first path and the strongest path is 60 ns, a window length larger than 60 ns may introduce the problem of regarding the channel tail as the leading edge. In Fig. 10, the window length of 60 ns maintains the best performance at high SNR. When the window length is 70 ns, there is a performance degradation. Since the threshold is low, the channel tail may cross the threshold to cause an estimation error. When the window length is 50 ns, an estimation error may occur, because the interval between the first and the strongest peak is larger than the window length.

When we observe the performance of the JBSF method using different thresholds $\gamma_2$ as a function of $P_{EFA}$ for a fixed window length $L_w = 50$ ns in Fig. 11, they all have
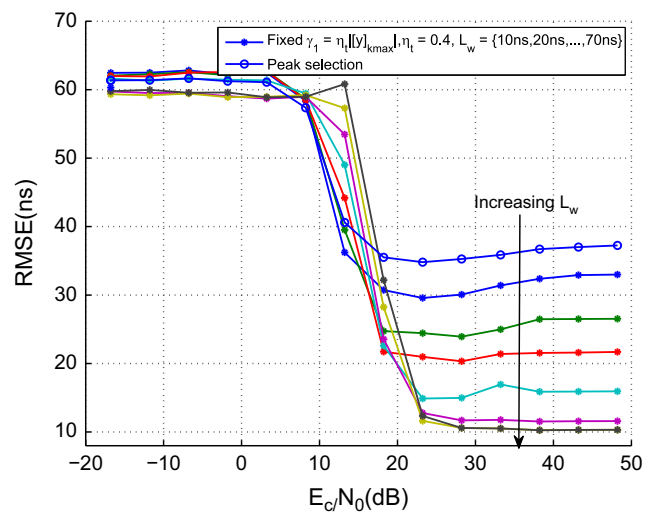


**Fig. 9.** RMSE of TOA estimation using the JBSF method for a fixed threshold $\gamma_1 = \eta_t |[\mathbf{y}]_{k_{max}}|$, $\eta_t = 0.4$ and different window lengths, $m = 7$.
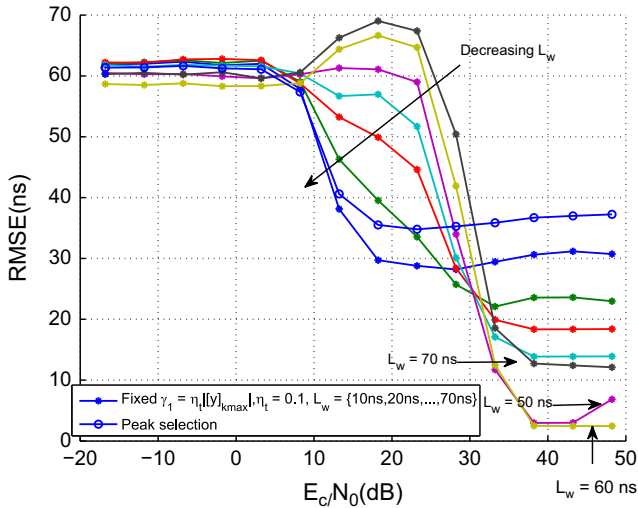
**Fig. 10.** RMSE of TOA estimation using the JBSF method for a fixed threshold $\gamma_1 = \eta_t |[\mathbf{y}]_{k_{max}}|$, $\eta_t = 0.1$ and different window lengths, $m = 7$.
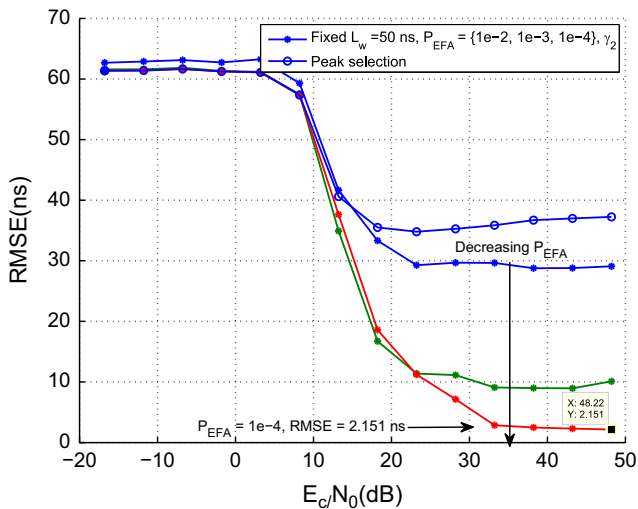


**Fig. 11.** RMSE of TOA estimation using the JBSF method for a fixed window length $L_w = 50$ ns and different thresholds $\gamma_2$, $m = 7$.
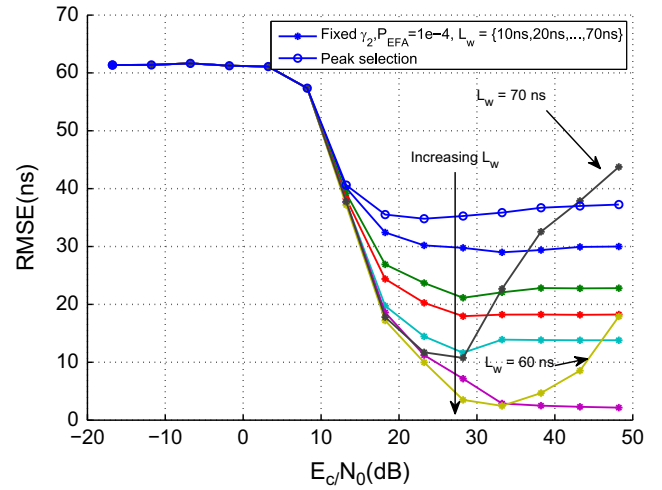


**Fig. 12.** RMSE of TOA estimation using the JBSF method for a fixed threshold $\gamma_2$, $P_{EFA} = 10^{-4}$ and different window lengths, $m = 7$.
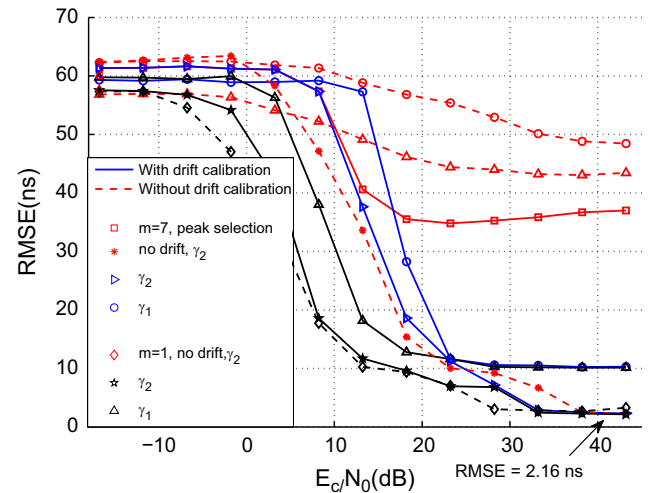


**Fig. 13.** RMSE of TOA estimation using the JBSF method, $L_w = 60$ ns, $\gamma_1 = \eta_t |[\mathbf{y}]_{k_{max}}|$, $\eta_t = 0.4$, and $L_w = 50$ ns, $\gamma_2$, $P_{EFA} = 10^{-4}$.

the same performance as the PS method in the SNR range of −17 to 13 dB. This is because in the low SNR range, the received signal is overwhelmed by noise. The chance of a sample value exceeding the threshold is low. As we use the result of peak selection when there is no threshold crossing, the performance of the JBSF method using $\gamma_2$ in the low SNR range is the same as the PS method. In the high SNR range, the smaller the $P_{EFA}$, the better the TOA estimate. The PS method still has the highest error floor. Further, we use a fixed threshold related to $P_{EFA} = 10^{-4}$ to test the estimation performance under different window lengths as shown in Fig. 12. The larger the window length, the lower the error floor. The exception happens when $L_w = 70$ ns and $L_w = 60$ ns. Then the search window is too long, and includes the channel tail, which causes an estimation error.

In Fig. 13, we finally compare the performance of the JBSF method for $\gamma_1 = \eta_t |[\mathbf{y}]_{k_{max}}|$, $\eta_t = 0.4$ with $L_w = 60$ ns, and $\gamma_2$, $P_{EFA} = 10^{-4}$ with $L_w = 50$ ns. There are still large

performance gaps between the methods with drift calibration and the ones without (dashed lines with "○" and "△" markers). We employ $\gamma_2$ for the cases of no drift (dashed lines with "∗" and "◇" markers), whose performance is similar as the ones using $\gamma_2$ for the cases with drift calibration (solid lines with "▷" and "★" markers). The SNR penalty of stroboscopic sampling ($m = 7$) compared to Nyquist rate sampling ($m = 1$) is again about 9 dB. In general, the PS method (the solid line with "□") has a much higher error floor than the JBSF method. The JBSF method using $\gamma_2$ and $L_w = 50$ ns (solid lines with "▷" and "★" markers) could converge to a lower error floor (2.16 ns) than the JBSF method using $\gamma_1$ and $L_w = 60$ ns (solid lines with "○" and "△" markers). Based on the above observations, we could employ the combination of $\gamma_2$, $P_{EFA} = 10^{-4}$ and $L_w = 50$ ns as a good option.

## 5. Conclusions

In this paper, we have adopted stroboscopic sampling as a practical low sampling rate solution for accurate TOA estimation using IR-UWB. Due to the long preamble required by stroboscopic sampling, the clock drift is one

of the main error sources in TOA estimation. Hence, we have included the drift into our system model and obtained a drift estimate through exhaustive search. Further, we have employed the PS and JBSF methods to estimate the TOA using the averaged data samples corrected for the drift. Simulation results confirm that drift calibration dramatically reduces the TOA estimation errors due to the drift, and stroboscopic sampling can achieve the same estimation resolution as Nyquist rate sampling.

## References

[1] Y. Wang, G. Leus, H. Delic, TOA estimation using UWB with low sampling rate and clock drift calibration, in: Proceedings of IEEE Conference UWB Systems & Technologies, Vancouver, Canada, 2009, pp. 612–617.

[2] J.-Y. Lee, R. Scholtz, Ranging in a dense multipath environment using an UWB radio link, IEEE Journal on Selected Areas in Communications 20 (9) (2002) 1677–1683.

[3] IEEE Working Group 802.15.4, Part 15.4: Wireless Medium Access Control (MAC) and Physical Layer (PHY) Specifications for Low-Rate Wireless Personal Area Networks (LR-WPANs).

[4] Z. Sahinoglu, S. Gezici, Ranging in the IEEE 802.15.4a standard, in: IEEE Annual Conference on Wireless and Microwave Technology, Clearwater Beach, FL, USA, 2006, pp. 1–5.

[5] S. Gezici, Z. Tian, G. Giannakis, H. Kobayashi, A. Molisch, H. Poor, Z. Sahinoglu, Localization via ultra-wideband radios: a look at positioning aspects for future sensor networks, IEEE Signal Processing Magazine 22 (July) (2005) 70–84, http://dx.doi.org/10.1109/MSP.2005.1458289.

[6] D. Dardari, A. Conti, U. Ferner, A. Giorgetti, M.Z. Win, Ranging with ultrawide bandwidth signals in multipath environments, Proceedings of IEEE 97 (2) (2009) 404–426, http://dx.doi.org/10.1109/JPROC.2008.2008846.

[7] J. Zhang, P.V. Orlik, Z. Sahinoglu, A.F. Molisch, P. Kinney, UWB systems for wireless sensor networks, Proceedings of IEEE 97 (2) (2009) 313–331, http://dx.doi.org/10.1109/JPROC.2008.2008786.

[8] I. Akyildiz, W. Su, Y. Sankarasubramaniam, E. Cayirci, A survey on sensor networks, IEEE Communications Magazine 40 (8) (2002) 102–114, http://dx.doi.org/10.1109/MCOM.2002.1024422.

[9] C.-Y. Chong, S. Kumar, Sensor networks: evolution, opportunities, and challenges, Proceedings of IEEE 91 (8) (2003) 1247–1256, http://dx.doi.org/10.1109/JPROC.2003.814918.

[10] R. Verdone, D. Dardari, G. Mazzini, A. Conti, Wireless Sensor and Actuator Networks: Technologies, Analysis and Design, Elsevier, Amsterdam, the Netherlands, 2008.

[11] R. Walden, Analog-to-digital converter survey and analysis, IEEE Journal on Selected Areas in Communications 17 (4) (1999) 539–550, http://dx.doi.org/10.1109/49.761034.

[12] B. Le, T. Rondeau, J. Reed, C. Bostian, Analog-to-digital converters, IEEE Signal Processing Magazine 22 (6) (2005) 69–77, http://dx.doi.org/10.1109/MSP.2005.1550190.

[13] C. Falsi, D. Dardari, L. Mucchi, M. Win, Time of arrival estimation for UWB localizers in realistic environments, EURASIP Journal on Applied Signal Processing (2006) 1–13.

[14] I. Guvenc, Z. Sahinoglu, P. Orlik, TOA estimation for IR-UWB systems with different transceiver types, IEEE Transactions on Microwave Theory and Techniques 54 (4) (2006) 1876–1886, http://dx.doi.org/10.1109/TMTT.2006.872044.

[15] I. Guvenc, Z. Sahinoglu, A. Molisch, R. Orlik, Non-coherent TOA estimation in IR-UWB systems with different signal waveforms, in: Second International Conference on Broadband Networks, 2005, BroadNets 2005, vol. 2, 2005, pp. 1168–1174. http://dx.doi.org/10.1109/ICBN.2005.1589740.

[16] I. Guvenc, Z. Sahinoglu, Threshold-based TOA estimation for impulse radio UWB systems, in: Proceedings of IEEE ICU, 2005, pp. 420–425. http://dx.doi.org/10.1109/ICU.2005.1570024.

[17] D. Dardari, C.-C. Chong, M. Win, Threshold-based time-of-arrival estimators in UWB dense multipath channels, IEEE Transactions on Communications 56 (8) (2008) 1366–1378, http://dx.doi.org/10.1109/TCOMM.2008.050551.

[18] A. D'Amico, U. Mengali, L. Taponecco, Energy-based TOA estimation, IEEE Transactions on Wireless Communications 7 (3) (2008) 838–847, http://dx.doi.org/10.1109/TWC.2008.060545.

[19] R. Zhang, X. Dong, A new time of arrival estimation method using UWB dual pulse signals, IEEE Transactions on Wireless Communications 7 (6) (2008) 2057–2062, http://dx.doi.org/10.1109/TWC.2008.070112.

[20] A.A. D'Amico, U. Mengali, L. Taponecco, TOA estimation with the IEEE 802.15. 4a standard, IEEE Transactions on Wireless Communications 9 (7) (2010) 2238–2247.

[21] A. Giorgetti, M. Chiani, Time-of-arrival estimation based on information theoretic criteria, IEEE Transactions on Signal Processing 61 (8) (2013) 1869–1879, http://dx.doi.org/10.1109/TSP.2013.2239643.

[22] K. Witrisal, G. Leus, G.J.M. Janssen, M. Pausini, F. Troesch, T. Zasowski, J. Romme, Noncoherent ultra-wideband systems, IEEE Signal Processing Magazine 26 (4) (2009) 48–66, http://dx.doi.org/10.1109/MSP.2009.932617.

[23] K. Gedalyahu, Y. Eldar, Time-delay estimation from low-rate samples: a union of subspaces approach, IEEE Transactions on Signal Processing 58 (6) (2010) 3017–3031, http://dx.doi.org/10.1109/TSP.2010.2044253.

[24] Z. Irahhauten, A. Yarovoy, G. Janssen, H. Nikookar, L. Ligthart, Suppression of noise and narrowband interference in UWB indoor channel measurements, in: Proceedings of IEEE International Conference on Ultra-Wideband, 2005, pp. 108–112. http://dx.doi.org/10.1109/ICU.2005.1569967.

[25] B. Zhen, H.-B. Li, R. Kohno, Clock management in ultra-wideband ranging, in: Mobile and Wireless Communications Summit, 2007, 16th IST, 2007, pp. 1–5. http://dx.doi.org/10.1109/ISTMWC.2007.4299163.

[26] A. Wellig, Y. Qiu, Trellis-based maximum-likelihood crystal drift estimator for ranging applications in UWB-LDR, in: Proceedings of IEEE International Conference on Ultra-wideband, 2006, pp. 539–544. http://dx.doi.org/10.1109/ICU.2006.281606.

[27] A. Wellig, Method and device for estimation the relative drift between two clocks, in particular for ranging applications in UWB-LDR technology, March 2008.

[28] W. Black, D. Hodges, Time interleaved converter arrays, IEEE Journal of Solid-State Circuits 15 (6) (1980) 1022–1029, http://dx.doi.org/10.1109/JSSC.1980.1051512.

[29] B. Razavi, Design of sample-and-hold amplifiers for high-speed low-voltage a/d converters, in: Custom Integrated Circuits Conference, 1997, Proceedings of the IEEE 1997, 1997, pp. 59–66. http://dx.doi.org/10.1109/CICC.1997.606585.

[30] M. Shinagawa, Y. Akazawa, T. Wakimoto, Jitter analysis of high-speed sampling systems, IEEE Journal of Solid-State Circuits 25 (1) (1990) 220–224, http://dx.doi.org/10.1109/4.50307.

[31] K. Poulton, J. Corcoran, T. Hornak, A 1-GHz 6-bit ADC system, IEEE Journal of Solid-State Circuits 22 (6) (1987) 962–970.

[32] D. Fu, K. Dyer, S. Lewis, P. Hurst, A digital background calibration technique for time-interleaved analog-to-digital converters, IEEE Journal of Solid-State Circuits 33 (12) (1998) 1904–1911, http://dx.doi.org/10.1109/4.735530.

[33] S. Kay, Fundamentals of Statistical Signal Processing, Detection Theory, vol. II, Prentice-Hall, 1993.

[34] S. Wu, Q. Zhang, R. Fan, N. Zhang, Match-filtering based TOA estimation for IR-UWB ranging systems, in: Proceedings of IEEE IWCMC, 2008, pp. 1099–1105. http://dx.doi.org/10.1109/IWCMC.2008.191.

[35] A. Molisch, K. Balakrishnan, C. Chong, S. Emami, A. Fort, J. Karedal, J. Kunisch, H. Schantz, U. Schuster, K. Siwiak, IEEE 802.15.4a Channel Model—Final Report, Technical Report, 2005.